

www.acsami.org Research Article

# Elucidating the Role of Electrochemically Formed LiF in Discharge and Aging of Li-CF<sub>x</sub> Batteries

Theresa Schoetz, Loleth E. Robinson, Leo W. Gordon, Sarah A. Stariha, Celia E. Harris, Hui Li Seong, John-Paul Jones, Erik J. Brandon, and Robert J. Messinger\*



Cite This: ACS Appl. Mater. Interfaces 2024, 16, 18722–18733



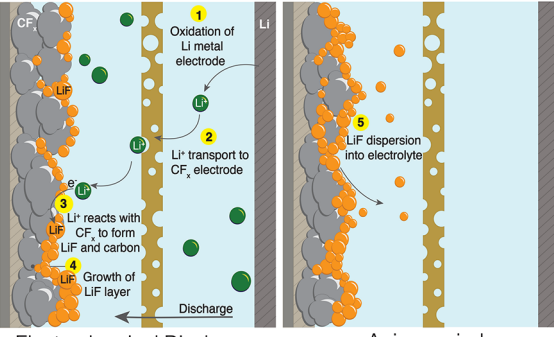
**ACCESS** I

III Metrics & More

Article Recommendations

Supporting Information

**ABSTRACT:** Fifty years after its introduction, the lithium-carbon monofluoride (Li-CF $_x$ ) battery still has the highest cell-level specific energy demonstrated in a practical cell format. However, few studies have analyzed how the main electrochemical discharge product, LiF, evolves during the discharge and cell rest periods. To fill this gap in understanding, we investigated molecular-level and interfacial changes in CF $_x$  electrodes upon the discharge and aging of Li-CF $_x$  cells, revealing the role of LiF beyond that of a simple discharge product. We reveal that electrochemically formed LiF deposits on the surface of the CF $_x$  electrode and subsequently partially disperses into the electrolyte to form a colloidal suspension during cell aging, as determined from galvanostatic electrochemical impedance spectroscopy (EIS), solid-state <sup>19</sup>F nuclear magnetic resonance (NMR), dynamic light scattering (DLS), and *operando* optical



Electrochemical Discharge

Aging period

light microscopy measurements. Electrochemical LiF formation and LiF dispersion into the electrolyte are distinct competing rate processes that each affect the cell impedance differently. Using knowledge of LiF dispersion and saturation, an in-line EIS method was developed to compute the depth of discharge of  $CF_x$  cells beyond coulomb counting. Solid-state <sup>19</sup>F NMR measurements quantitatively revealed how LiF and CF moieties evolved with discharge. Covalent CF bonds react first, followed by a combination of covalent and ionic CF bonds. Quantitively correlating NMR and electrochemical measurements reveals not only how LiF formation affects cell impedance but also that CF bonds with the most ionic character remain unreacted, which limits realization of the full theoretical specific capacity of the  $CF_x$  electrode. The results reveal new insights into the electrochemical discharge mechanism of Li- $CF_x$  cells and the unique role of LiF in cell discharge and aging, which suggest pretreatment strategies and methods to improve and measure the performance of Li- $CF_x$  batteries.

KEYWORDS: lithium batteries, primary batteries, lithium fluoride, carbon monofluoride, colloid, electrochemical impedance spectroscopy, solid-state nuclear magnetic resonance

# **■** INTRODUCTION

Lithium-carbon monofluoride (Li-CF<sub>r</sub>) batteries are among the highest energy density batteries known, both from a practical and theoretical standpoint, and are of significant technological interest when a high specific energy, nonrechargeable power source is needed. Accordingly, there is currently significant renewed interest in the Li-CF<sub>x</sub> battery chemistry, including a revisiting of its still poorly understood discharge mechanism, 1,2 the design of new higher-energy catholyte-based systems, 2-5 a re-evaluation for potential rechargeability, 6,7 and its consideration for challenging new applications requiring a very high specific energy battery option. <sup>1,8,9</sup> When  $CF_x$  is fluorinated (x = 1), they exhibit the highest theoretical specific capacity (865 mAh g<sup>-1</sup>, based on  $CF_x$  cathode) and highest theoretical specific energy (2180 Wh kg<sup>-1</sup>, based on a theoretical discharge potential of 4.57 V) on a materials basis among all commercialized lithium primary battery chemistries. The electrochemically active CF<sub>x</sub> powder is synthesized by the reaction of fluorine gas and carbon powder at high temperatures. Upon fluorination, an sp³-hybridized carbon structure is formed, with fluorine atoms bonded to the carbon atoms in a layered structure. The electronic conductivity and specific capacity of the  $CF_x$  electrode depends upon the level of fluorination, i.e., the value of x, which typically ranges from 0.9 to 1.2. As the fluorine content increases, the nature of the C-F bond shifts from ionic to covalent,  $^{11,12}$  a behavior attributed to the ability of fluorine to form both ionic and covalent bonds with carbon.  $^{13}$ 

Received: November 22, 2023
Revised: March 8, 2024
Accepted: March 18, 2024
Published: April 8, 2024





Li-CF<sub>x</sub> batteries can be found in a wide variety of applications that require very high specific energy and low self-discharge, yet do not require rechargeability, such as certain devices for medical, marine, military, or space applications. 1,14-16 For example, planetary science missions performed by robotic spacecraft are limited in scope by the performance of the current electrochemical energy storage systems available, where established chemistries are unable to adequately meet mission requirements. The development of high specific energy (>700 Wh kg<sup>-1</sup> at 25 °C) primary batteries with low self-discharge rates ( $\leq 0.5\%$  per year), coupled with radiation tolerance (10 Mrad total ionizing doses), could enable entirely new missions performing civilization-scale science on planetary bodies.<sup>17</sup> Despite the impressive specific energy of current Li-CF<sub>x</sub> battery cells at >700 Wh kg $^{-1}$ , it is far lower than its theoretical value. In particular, the theoretical discharge potential is 4.57 V, while the typical operating discharge potential is between 2.5 and 2.6 V. Such large overpotentials are, in part, due to the activation energy associated with breaking the C-F bond. Further scientific understanding and technological development of the Li-CF<sub>x</sub> battery chemistry could significantly enhance the scope and ambition of future planetary science missions.

During discharge, Li-CF, undergoes an exothermic electrochemical conversion reaction where the C-F bond breaks (eq 1), transforming the fluorinated carbon, CF<sub>x</sub>, into lithium fluoride, LiF, and carbon, C, at the cathode. Note that LiF is both an ionic and an electronic insulator, which can increase resistance, impede Li+ cation permeation, and electronically isolate CF<sub>x</sub> particles during electrochemical discharge. Simultaneously, metallic lithium, Li, is oxidized to Li<sup>+</sup> at the anode (eq 2). The half-cell and overall electrochemical discharge reactions are listed in eq 3.

cathode half-cell reaction:

$$CF_x + xLi^+ + xe^- \xrightarrow{\text{discharge}} xLiF + C$$
 (1)

anode half-cell reaction:

$$Li \xrightarrow{discharge} Li^{+} + e^{-}$$
 (2)

overall reaction:

$$CF_x + xLi \xrightarrow{discharge} xLiF + C$$
 (3)

Despite the very high specific energy density of Li-CF<sub>x</sub> batteries, much remains to be understood about their electrochemical discharge mechanism. Several discharge mechanisms have been proposed, from the direct formation of LiF to the formation of an intermediate compound structure. <sup>1,6,10,18–23</sup> In 1975, Whittingham et al. first proposed a two-phase reaction mechanism in which lithium ions intercalate between the fluorinated graphite sheets forming a nonstoichiometric ternary compound (CLixF). After discharge, X-ray diffraction (XRD) measurements of the cathode structure demonstrated a 3.55 Å increase in the interlayer spacing. Whittingham et al.<sup>24</sup> attributed the lattice expansion to a change in C-F bond nature from covalent to ionic due to the presence of an intercalated alkali metal. However, the intermediate compound was not observed experimentally. Watanabe et al.<sup>22</sup> also observed an expansion of the  $CF_x$ interlayer spacing, with two new signals at 688.3 and 687.0 eV in the  $F_{1s}$  electron spectroscopy for chemical analysis (ESCA) spectra, and one additional ESCA signal at 51 eV Li<sub>1s</sub> after

discharge, with the new features assumed to be from a nonstoichiometric intermediate compound, CLi<sub>x</sub>F<sub>v</sub>. Touhara et al. 18 proposed a solvent-mediated ternary compound, CFLi<sub>x</sub>/S<sub>v</sub> product due to the co-intercalation of both lithium ions and solvent molecules into the layered cathodic structure. Since the intermediate compound decomposes gradually into the final discharge products, the Gibbs free energy of formation of LiF and carbon is only partially transformed into electrochemical potential resulting in a lower OCP. Guérin et al.<sup>21</sup> and Nagasubramanian et al.<sup>25</sup> report the formation of a LiF layer outside of the carbon lattice, which increases in thickness during discharge. Read et al. suggest a direct two-phase reaction in which amorphous LiF initially deposits on the carbon structure and later dissolves to recrystallize elsewhere in the carbon shell or organic electrolyte. The authors suggested that LiF particles undergo Ostwald ripening within the carbon shell after recrystallization, explaining the swelling of the cathode. It is evident that a quantitative molecular-level understanding of the electrochemical defluorination mechanism has not yet been elucidated. In particular, understanding the role of LiF, <sup>26–28</sup> including its distribution in the cell and its evolution with aging is critical to understanding the performance of the cell, in particular with respect to long-term storage.

Here, we investigate molecular-level and interfacial changes in CF<sub>x</sub> electrodes upon electrochemical discharge and aging through correlated electrochemical impedance spectroscopy (EIS) and solid-state nuclear magnetic resonance (NMR) measurements. The measurements show that interfacial LiF at the CF<sub>r</sub> electrode disperses into the electrolyte and forms a colloidal suspension during cell aging. Dynamic light scattering (DLS) and light microscopy imaging further validate the dispersal of both crystalline LiF and electrochemically formed LiF into the electrolyte, respectively. The discovery elucidates that electrochemically formed LiF on the CF<sub>x</sub> electrode during discharge is accompanied by competing dispersion into the electrolyte, changing the thermodynamic characteristics of the CF<sub>x</sub> electrode during aging and discharge. We use this new insight to determine the depth of discharge of the Li-CF<sub>x</sub> battery, which can be experimentally challenging compared to other lithium-based batteries, by eliminating the so far unknown LiF dispersion process during battery pretreatment. In so doing, we were able to determine the growth function of electrochemically formed LiF with in-line EIS during discharge. Ultimately, we leverage the molecular-level mechanistic insights for an application-orientated use and demonstrate a new piece of knowledge to the overall discharge mechanism of the Li-CF<sub>x</sub> battery chemistry.

#### **EXPERIMENTAL METHODS**

Electrode and Cell Preparation. The CF<sub>x</sub> cathodes were prepared in-house by mixing 92% CF<sub>x</sub> powder (ARC,  $x \approx 1$ , theoretical capacity of 865 mAh g<sup>-1</sup>), 5% carbon black (Super P, Alfa Aesar), and 3% poly(vinylidene fluoride) (Sigma-Aldrich). The CF<sub>x</sub> slurry was cast on a 0.025 mm thick aluminum foil (Shop-Aid, Inc.) precoated with a layer of carbon ink (EB-012 Henkel Corp). The composite CF<sub>x</sub> cathode loading was 11.27 mg cm<sup>-2</sup>. Li metal electrodes (China Lithium Products Technology) with a thickness of 0.017 mm were gently scraped with a metal spatula to remove any surface impurities. Stainless steel CR2032 coin cells were prepared with 16 mm dried CF<sub>x</sub> cathodes and free-standing Li metal anodes, 17 mm separators (Celgard 2325) and 100  $\mu$ L of electrolyte consisting of 0.75 M LiBF4 in propylene carbonate (Mitsubishi, F-grade) and dimethoxyethane (PC/DME) (Mitsubishi, F-grade) with a 3:7 volume ratio, under argon atmosphere  $(H_2O, O_2 < 1 \text{ ppm})$ .

Following crimp sealing, all coin cells were additionally sealed with epoxy (JB Weld) to avoid potential exposure to air when handled outside the glovebox.

Three-electrode cells were prepared using dried  $CF_x$  cathodes prepared in-house using the same composition, mass loading, and substrate described above but cut into rectangular dimensions of 135 mm  $\times$  40 mm. Lithium metal anodes were prepared by pressing a rectangular 140 mm  $\times$  40 mm piece of lithium metal foil (Foote Mineral Company) on 0.025 mm thick copper foil (Shop-Aid, Inc.). The reference electrode was prepared by pressing lithium metal foil on a nickel mesh and welding it to a nickel tab. The three-electrode cells were wrapped in separator sheets (Celgard 2325), stacked, and tightly rolled around a PTFE mandrel. The roll was placed inside a glass vial and filled with 4 mL of electrolyte inside an argon-filled glovebox ( $H_2O$ ,  $O_2 < 1$  ppm). The roll was placed inside a glass vessel and electrical leads were connected to the assembly. A detailed schematic of the spiral wound three-electrode cell and its fabrication has been previously published by Jow et al.

The cells were then discharged to 3% DOD at a rate of C/120 at 20 °C, heat-treated at 55 °C for 40 h, and then aged between 1 and either 35 or 42 days at 20 °C, respectively, for two- or three-electrode cells. The heat treatment step is necessary to establish a well-defined lithium anode passivation layer and stabilize the open-circuit potential and self-discharge rate. Galvanostatic discharging was performed using an Arbin LBT battery tester, where cell temperatures were controlled using an Arbin multizone temperature chamber. All specific capacities are reported per mass of  $CF_x$ . DOD is defined based on the theoretical capacity of a  $CF_x$  electrode (x = 1), or 865 mAh g<sup>-1</sup>.

Nuclear Magnetic Resonance Spectroscopy. Solid-state NMR experiments were performed on a Bruker Avance III HD NMR spectrometer with a 14.1 T narrow bore (51 mm) superconducting magnet equipped operating at 564.70 and 233.24 MHz for <sup>19</sup>F and <sup>7</sup>Li nuclei, respectively. A PhoenixNMR 1.6 mm HXY MAS probe head was used, where all measurements were conducted with magic-anglespinning (MAS) rates of 40 kHz. Air was pumped through the probe head at 298.2 K and 600 L h<sup>-1</sup> to mitigate sample heating due to MAS. All solid-state <sup>19</sup>F and <sup>7</sup>Li NMR experiments used rf field strengths of 152 kHz ( $\pi/2$  of 1.65  $\mu$ s) and 125 kHz ( $\pi/2$  of 2.0  $\mu$ s), respectively, for all broadband rf pulses. To reduce 19F probe background signals, all solid-state <sup>19</sup>F NMR measurements were performed using spin-echo experiments with a rotor-synchronized delay of 1 rotor period between the  $\pi/2$  and  $\pi$  pulses (full-echo delay of 50  $\mu$ s). For solid-state  $^{7}$ Li NMR experiments, single-pulse experiments were performed. All solid-state 19F and 7Li NMR experiments were performed under quantitative conditions using recycle delays of 60 s, during which all nuclear spins relaxed to thermal equilibrium (>5  $\times$   $T_1$ , the longitudinal relaxation time). Note that the 19F spin-echo experiments are, to an excellent approximation, quantitative as the full-echo delay of 50  $\mu s$  was much less than the <sup>19</sup>F transverse relaxation times  $(T_2)$ , which ranged from 1.50 to 6.74 ms. <sup>19</sup>F and <sup>7</sup>Li chemical shifts were referenced to CFCl<sub>3</sub> at 0 ppm and 1 M aqueous LiNO<sub>3</sub> at 0 ppm, respectively, using pristine LiF (Sigma-Aldrich, ≥99.99%) as a secondary chemical shift reference with a <sup>19</sup>F shift of -204 ppm and a <sup>7</sup>Li shift of -1 ppm. Solid-state NMR spectra were deconvoluted using DMFit.<sup>30</sup>

For solid-state NMR sample preparation,  $\overline{CF_x}$  electrodes were harvested from coin cells inside an argon-filled glovebox ( $H_2O$ ,  $O_2 < 1$  ppm). Coin cells were decrimped using an MTI electric decrimping machine, where the decrimping pressure was set to 2016 psi. The  $\overline{CF_x}$  active material was removed from the aluminum current collector and mixed with barium fluoride ( $\overline{BaF_2}$ ), 1:2 by weight.  $\overline{BaF_2}$  was used as an internal standard for quantifying the total  $^{19}F$  signal intensity as well as an additional internal  $^{19}F$  chemical shift reference. Quantification of the absolute  $^{19}F$  signal using  $\overline{BaF_2}$  as a reference, normalized by sample mass, did not scale as expected. This result may be due to differences in densities of the  $\overline{CF_x}$  electrodes upon electrochemical discharge. Nevertheless, the solid-state  $^{19}F$  MAS NMR spectra were calibrated to be quantitative with regard to the relative  $^{19}F$  signal intensities of the different moieties, as indicated by the excellent agreement between the relative quantity of LiF formed

and the DOD with respect to the theoretical specific capacity (see below).

Liquid-state NMR experiments were performed on a Bruker AVANCE NEO 600 NMR spectrometer with a 14.1 T narrow bore (51 mm) superconducting magnet operating at 564.64 and 233.23 MHz for  $^{19}\mathrm{F}$  and  $^7\mathrm{Li}$  nuclei, respectively. A Bruker 5 mm double-resonance DiffBB probe (DIFF-DR-BB/1H&19F-D-Z-5 mm) was used for all measurements. All liquid-state single-pulse NMR spectra were acquired under quantitative conditions (recycle delays > 5 ×  $T_1$ , the longitudinal relaxation time) using rf field strengths of 11.4 kHz ( $\pi/2$  of 22.0  $\mu$ s) and 15.6 kHz ( $\pi/2$  of 16.0  $\mu$ s), for  $^{19}\mathrm{F}$  and  $^7\mathrm{Li}$  nuclei, respectively. Samples were prepared with a 3 mm coaxial capillary tube containing a solution of 0.75 M LiTFSI in D<sub>2</sub>O as an internal spin-counting reference for signal quantification.

Electrochemical Impedance Spectroscopy. Galvanostatic EIS (GEIS) measurements were performed using a 100 μA perturbation signal around a base current of 0 mA from 10 Hz to 100 kHz (Biologic VSP-300 potentiostat) at ambient temperature. The GEIS measurements were performed on both three-electrode cells and twoelectrode coin cells. Three-electrode measurements were performed in a glass cell with lithium foil on Ni mesh as a quasi-reference electrode and assembled under argon atmosphere (H2O, O2 < 1 ppm). In-line EIS was performed on two-electrode coin cells immediately after a constant current discharge step. Before each measurement, the three-electrode cells and two-electrode coin cells rested for 4 h until they reached a stable OCP with  $\Delta E$  < 0.01 V. The data and individual circuit components of the complex plane plots were fitted and quantitatively disentangled using a custom MATLAB code (Supporting Information). Real parts of the impedance values were obtained by determining the diameter of the fitted semicircles, modeled by a Q/R element.

Potentiostatic EIS (PEIS) at 10 mV perturbation signal around a base potential of 0 V from 1 Hz to 500 kHz (Biologic VSP-300 potentiostat) was used to measure the specific conductivities of electrolyte mixtures. The electrolyte containing 0.75 M LiBF $_4$  in PC/DME with a 3:7 volume ratio was mixed with 0.1–2 M of LiF (Sigma-Aldrich,  $\geq$ 99.99%) for a period of 8 days inside an argon-filled glovebox (H $_2$ O, O $_2$  < 1.0 ppm). Approximately 0.6 mL of the electrolyte and electrolyte mixtures were transferred to a conductivity cell and sealed inside the argon-filled glovebox. The conductivity cell (BioLogic) consists of two parallel platinum electrodes with a rubber sealing cap. Once sealed, the conductivity cell was placed inside an environmental chamber (BTZ133, Espec) to control the temperature at 25 °C.

**Dynamic Light Scattering.** Changes in the LiF particle size, when immersed in the electrolyte containing 0.75 M LiBF<sub>4</sub> in PC/DME with a 3:7 volume ratio, were determined by DLS measurements (Malvern Zetasizer Nano ZS). Crystalline LiF (Sigma-Aldrich,  $\geq$ 99.99%) with an average initial particle size between 50 and 100  $\mu$ m was mixed with the electrolyte (7.78 mg in 3 mL) aiming for a 0.1 M dispersion. The particle size was determined after mixing the solutions for 6 h, 3 days, or 8 days.

**Optical Light Microscopy.** Changes in the  $CF_x$  electrode surface morphology during the aging period were observed by *operando* optical light microscopy. A 50× objective on a BX51RF Olympus microscope was used for data acquisition. A coin cell was galvanostatically discharged to 3% DOD, heat-treated, and then disassembled by decrimping of the cell. The  $CF_x$  electrode was then immersed in the electrolyte, 0.75 M LiBF<sub>4</sub> in PC/DME with a 3:7 volume ratio, and hermetically sealed under argon between two microscopy glasses. The airtight microscopy setup was constructed using epoxy (J-B Weld Clearweld, Devcon 5 min epoxy gel), poly(methyl methacrylate), microscope slides (Thermo Fisher Scientific), and microscope cover glass (Thermo Fisher Scientific, no. 1 thickness). Optical images of the exact same surface area on the  $CF_x$  electrode were then taken between 9 and 14 days of aging.

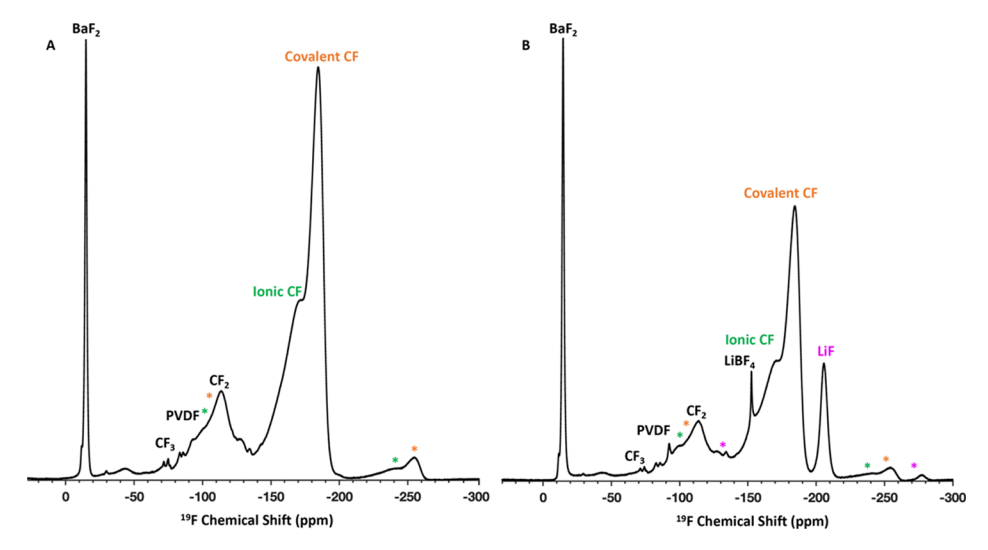


**Figure 1.** Solid-state <sup>19</sup>F MAS NMR spectra of (A) pristine CF<sub>x</sub> electrode and (B) CF<sub>x</sub> electrode discharged to 4% DOD acquired at 14.1 T and 40 kHz MAS. Spinning side bands are labeled with asterisks and are color-coded as follows: ionic CF is green, covalent CF is orange, and LiF is pink. BaF<sub>2</sub> was added as an internal <sup>19</sup>F reference.

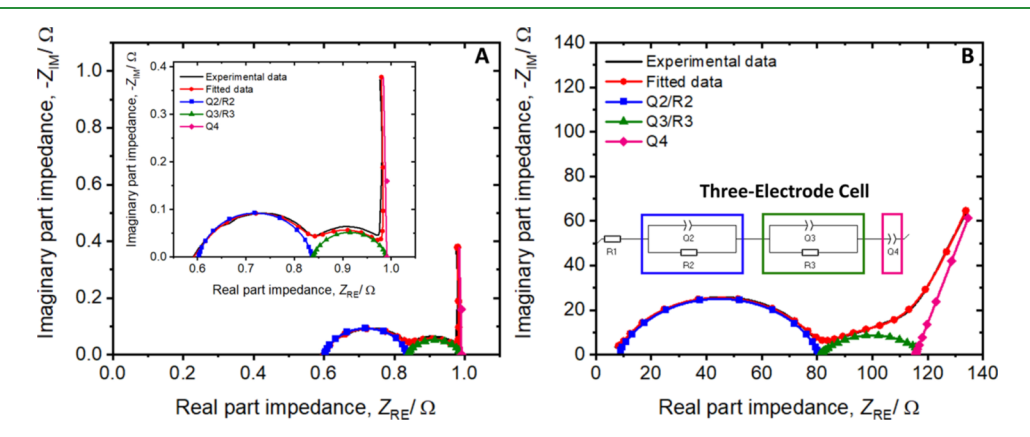


Figure 2. EIS complex plane plot of (A) a  $CF_x$  electrode discharged to 30% DOD in a three-electrode cell configuration (inset: enlarged complex plane plot) and (B) Li- $CF_x$  two-electrode cell discharged to 75% DOD with disentangled equivalent circuit elements, respectively (inset: equivalent circuit used to model the EIS data).

### ■ RESULTS AND DISCUSSION

# Formation of the LiF Interface in the CF<sub>x</sub> Cathode.

When a Li-CF<sub>x</sub> cell discharges, it forms LiF as a discharge product on CF<sub>x</sub> particles in the cathode (eq 1). LiF is not electrically or ionically conductive<sup>31</sup> and therefore gradually forms a blocking layer around the CF<sub>x</sub> particles that becomes progressively more resistive for lithium ions with increasing DOD. The permeability and conductivity of the LiF layer depend on its thickness, homogeneity, and porosity. The LiF coverage in Li-CF<sub>x</sub> cells is generally inhomogeneous and thus the cathode remains partially electrically conductive and permeable for Li<sup>+</sup> ions with increasing DOD.  $^{1,21}$ 

To identify electrochemically formed LiF and the main fluorine environments in  $CF_x$  electrodes, solid-state <sup>19</sup>F MAS NMR spectra were acquired under quantitative conditions on a pristine  $CF_x$  electrode and a  $CF_x$  electrode discharged to 4% DOD (Figure 1). The solid-state <sup>19</sup>F NMR spectrum of the pristine  $CF_x$  electrode (Figure 1A) reveals an intense <sup>19</sup>F signal at -184 ppm attributed to covalent CF groups, <sup>32,33</sup> while the unresolved <sup>19</sup>F signal centered at -170 ppm is associated with ionic CF. <sup>34</sup> The ionic C–F bonds <sup>35,36</sup> could also be described as covalent in nature, with a contribution from hyperconjugation. Hyperconjugation within the C–C bonds of the

 $\mathrm{CF}_x$  structure effectively lowers the C–F bond order, resulting in a distortion of its covalent nature. The broad  $^{19}\mathrm{F}$  signal around -112 ppm is attributed to CF2 signals on graphite sheet edge sites, while multiple weak, well-resolved  $^{19}\mathrm{F}$  signals clustered between -70 and -90 ppm are associated with CF3 surface sites. The  $^{19}\mathrm{F}$  signal at -92 ppm, which is more resolved in the discharged CFx electrode, is due to the PVDF binder. PVDF binder exhibits multiple  $^{19}\mathrm{F}$  signals that depend upon its local structure. The dominant  $^{19}\mathrm{F}$  PVDF resonance has been reported to be -91 ppm and corresponds to amorphous domains. The  $^{19}\mathrm{F}$  PVDF signals overlap with CF2 sites, but are weak in intensity, as PVDF consists of only 3 wt % of the composite electrode.

After discharge to 4% DOD, the solid-state <sup>19</sup>F NMR spectrum (Figure 1B) reveals that a well-resolved <sup>19</sup>F signal appears at -204 ppm, which is attributed to the electrochemically formed LiF (eq 1). Solid-state <sup>19</sup>F NMR spectra were also acquired at slower MAS rates of 25 kHz to aid in the identification of isotropic <sup>19</sup>F CF<sub>2</sub> and CF<sub>3</sub> signals, as the spinning side bands from the CF moieties overlap differently with these signals at different MAS rates (Figure S1, Supporting Information). The <sup>19</sup>F signals associated with the covalent and ionic CF groups decrease during discharge as

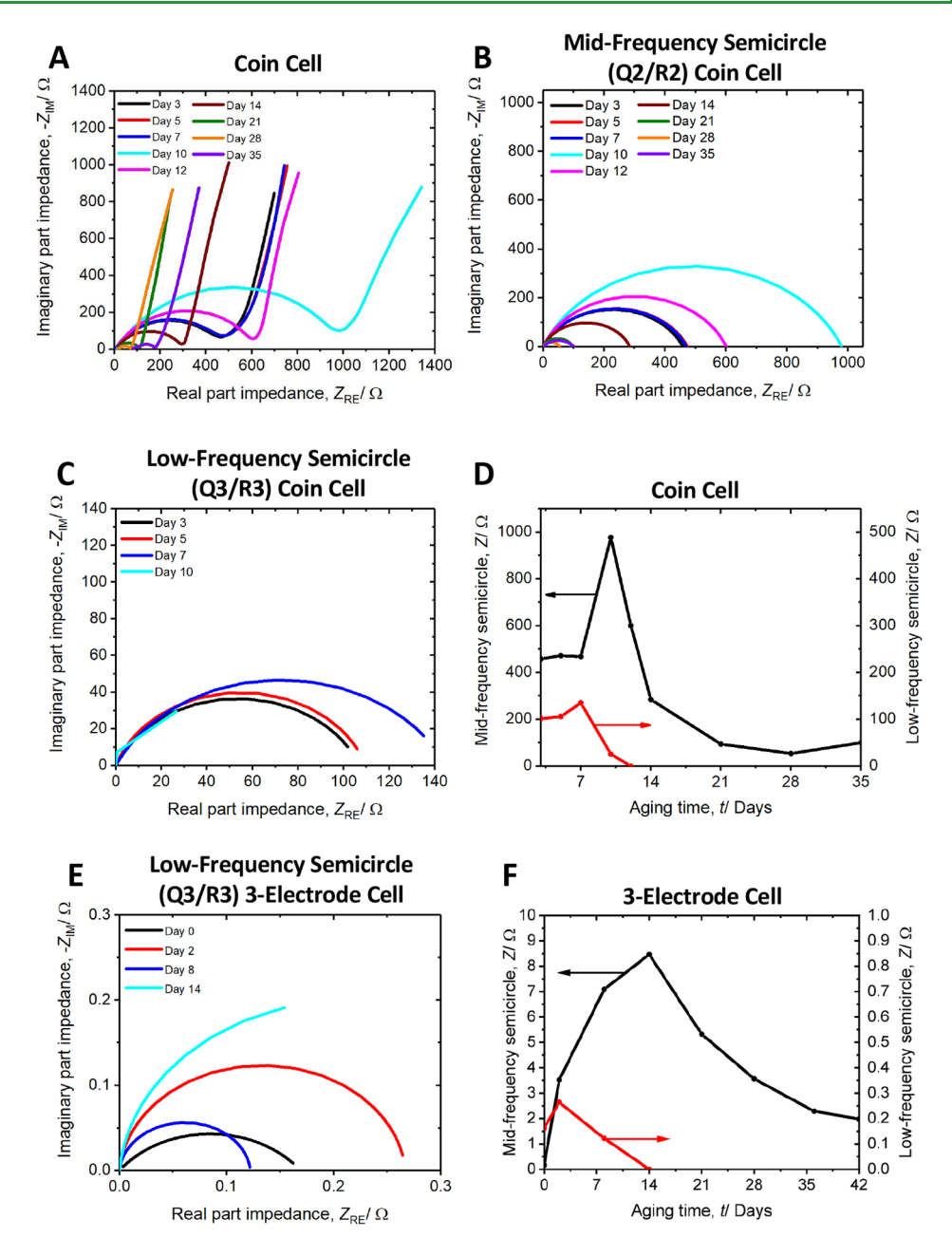


Figure 3. (A) EIS complex plane plot of Li-CF<sub>x</sub> two-electrode coin cells discharged to 3% DOD and aged for up to 35 days. Disentangled (B) mid-frequency  $(Q_2/R_2)$  and (C) low-frequency  $(Q_3/R_3)$  semicircles for the two-electrode coin cells. The low-frequency semicircle disappeared after 10 days of aging. (D) Impedance of the mid-frequency and low-frequency semicircles of the coin cell setup after different aging times. (E) Disentangled low-frequency semicircle for the three-electrode cells. (F) Impedance of the mid-frequency and low-frequency semicircles of the three-electrode cells after different aging times. The low-frequency semicircle disappeared after 14 days of aging.

they react to form LiF. The  $CF_x$  electrodes were not rinsed prior to performing solid-state NMR measurements to avoid any potential interactions with the solvent. Accordingly, a sharp <sup>19</sup>F signal at -154 ppm attributed to residual LiBF<sub>4</sub> salt was observed in the  $CF_x$  electrode discharged to 4% DOD. Thus, solid-state <sup>19</sup>F NMR measurements show that the expected electrochemical discharge mechanism occurs (eq 1), which involves C-F bond breaking and the electrochemical formation of LiF.

EIS was used to track interfacial changes in the  $\operatorname{CF}_x$  electrode as a function of aging and DOD, revealing the role of LiF. First, to identify, assign, and quantitatively disentangle the different EIS features, the complex plane plot of a  $\operatorname{CF}_x$ 

electrode discharged to 30% DOD in a three-electrode setup is analyzed in detail (Figure 2A). The complex plane plot exhibits one mid-frequency semicircle ( $Q_2/R_2$ , blue), associated with cathode impedance. When the Li-CF<sub>x</sub> battery is discharged, a low-frequency semicircle ( $Q_3/R_3$ ) arises in the complex plane plot. As shown below, this low-frequency semicircle is associated with LiF deposited on the surface of the CF<sub>x</sub> electrode, which forms a new interface between CF<sub>x</sub> and the organic electrolyte. As noted above, LiF is nonconductive and therefore gradually forms an inhomogeneous layer around the CF<sub>x</sub> particles, which becomes progressively resistive and thus harder for lithium ions to permeate with increasing DOD. The low-frequency impedance element ( $Q_4$ ), following the LiF low-

frequency semicircle, describes the ionic electrolyte species in the electrolyte at the electrode surface. To further demonstrate the presence of the low-frequency semicircle, representing the LiF layer on  $\operatorname{CF}_x$  electrodes, the same complex plane plots were fitted with only one Q/R element (Figure S2) displaying a poor fit.

EIS was also conducted on two-electrode coin cells to further corroborate the results of the three-electrode cells. Three-electrode cells were used to initially investigate any impedance changes at the CF<sub>x</sub> electrode. However, to analyze impedance changes that occur in the battery during galvanostatic discharge, two-electrode coin cells were also studied. The three- and two-electrode impedance data are compared and analyzed in the Supporting Information (Figure S3). Unlike in a three-electrode system, where the midfrequency semicircle  $(Q_2/R_2)$  represents only impedance contributions from the CF<sub>x</sub> electrode, the mid-frequency semicircle in the two-electrode setup (Figure 2B) also includes impedances that originate from the Li metal electrode, including the primitive SEI-type film that forms on the lithium metal surface. Previous studies have demonstrated depassivation of the lithium metal film in the Li-CF<sub>x</sub> system even at very low current densities (ca. 0.01 mA cm<sup>-2</sup>). The low-frequency semicircle  $(Q_3/R_3)$  in a two-electrode cell contains impedances associated with both the LiF layer and the mixed regime of the SEI (Figure S3A, Supporting Information). The impedance change of the mixed SEI regime is negligible with increasing cell age and DOD (Figure S3B,C, Supporting Information). Therefore, the only significant change associated with the lowfrequency semicircle in a two-electrode cell is related to the LiF layer at the cathode.

Aging of Cell Impedance and the LiF Interface. To investigate any changes to the LiF layer during cell aging, Li-CF<sub>r</sub> cells were discharged to 3% DOD to form LiF, heattreated at 55 °C for 40 h, and then subjected to EIS at different aging periods of up to 35 or 42 days for the two- or threeelectrode cells, respectively. Here, the real part of the impedance values of each Q/R element were obtained by determining the diameter of the fitted semicircle. The complex plane plots of the two-electrode Li-CF<sub>x</sub> coin cells (Figure 3A) show significant changes over the aging period, displaying nonmonotonic behavior indicative of competing rate processes. The real part impedance of the mid-frequency semicircle  $(Q_2/R_2)$  (Figure 3B) reaches a maximum after 10 days, whereafter it decreases gradually over the aging period. Interestingly, the low-frequency semicircle  $(Q_3/R_3)$  (Figure 3C) also increases at first over 7 days, but then decreases after 10 days of aging and subsequently completely disappears thereafter (Figure 3D). During aging when no current is passed, we hypothesize that the impedance increases due to local restructuring of the CFx interface but decreases due to LiF dispersion into the electrolyte, resulting in an impedance maximum that is observed after day 10. This observation is unexpected as LiF has been perceived as (electro)chemically stable in the electrolyte. The disappearance of the lowfrequency semicircle indicates that the LiF interface around the  $CF_x$  particles undergoes significant changes, giving rise to the hypothesis that LiF was dispersing into the electrolyte and therefore decreasing the overall interfacial resistance of the CF<sub>x</sub> electrode. Thus, despite the expectation that LiF will form an (electro)chemically stable layer around the CF<sub>x</sub> particles, we observed that the low-frequency semicircle in the complex plane plot, associated with the LiF interface around  $CF_{xy}$  disappears after 10 days of battery aging.

The EIS data of the  $CF_x$  electrode in three-electrode cells revealed the same trend (Figure 3E,F). The low-frequency semicircle  $(Q_3/R_3)$  disappears after 14 days of aging while the mid-frequency semicircle  $(Q_2/R_2)$  reaches a maximum at 14 days. Partial low-frequency semicircles were obtained at days 10 (two-electrode cell, Figure 3C) and 14 (three-electrode cell, Figure 3E) of aging, respectively. A full semicircle in a complex plane plot typically represents an interface in the electrochemical system; the disappearance of the full semicircles in both the two-electrode and three-electrode cells both suggest that the interface formed by the LiF layer disappears during the aging period. As shown below, the disappearance of the low-frequency semicircles  $(Q_3/R_3)$  is due to the gradual dispersion of the LiF layer into the electrolyte.

**Evolution of LiF during Aging.** To study how LiF interacts with the organic electrolyte during aging, we added crystalline LiF in different targeted concentrations (0.5–2 M) to the pristine electrolyte and measured the specific conductivity by EIS and the particle size by DLS. Surprisingly, we observed that LiF disappeared visually up to a concentration of approximately 1 M with and without stirring with a magnetic bar. The specific conductivity (Figure S4A) of the electrolyte changed by a negligible amount upon LiF addition, which would be expected to change significantly if the LiF salt dissociated into Li<sup>+</sup> cation and F<sup>-</sup> anions at the molecular level.

Liquid-state <sup>7</sup>Li and <sup>19</sup>F NMR measurements of the pristine electrolyte, as well as the electrolyte aged for 24 h after the addition of 1 M LiF, were acquired under quantitative conditions with an internal standard (Figure S5). The liquid-state NMR spectra do not reveal (i) the appearance of any additional <sup>19</sup>F or <sup>7</sup>Li signals, which would indicate new molecular-level environments or species, (ii) any significant changes in <sup>19</sup>F or <sup>7</sup>Li signal intensities, which would be expected if LiF was solubilizing at the molecular level, or (iii) any significant impact on the <sup>19</sup>F or <sup>7</sup>Li shifts. Thus, the liquid-state NMR measurements establish that the LiF is not solubilizing at a molecular level, a result corroborated by the specific conductivity measurements above. Note that the samples were visibly clear, while any solid LiF particles would not be detectable in liquid-state NMR measurements.

DLS measurements (Figure 4A), however, reveal that the particle size of crystalline LiF with a  $\leq 100 \ \mu m$  diameter decreases significantly to diameters ranging from 250 to 550 nm within 6 h of mixing LiF and electrolyte without stirring. After an aging period of 3 days, a bimodal particle size distribution was observed, with one population from 0.55 to 1.5 nm and another in the range of 300 nm-1  $\mu$ m. After 8 days, no particles were detected by DLS. However, we observed a hazy gel-like deposit at the bottom of the cuvette after 8 days (Figures 4B and S6), which lies outside the DLS beam. The liquid-state NMR and specific conductivity measurements prove that LiF exhibits only minute solvation in our electrolyte, consistent with previous literature that indicates that LiF has a solubility of 0.14 g L<sup>-1</sup> propylene carbonate. 40 We hypothesize that LiF disperses into the electrolyte and forms a colloidal dispersion upon aging. A colloid is a suspension of particles with characteristic dimensions smaller than 1000 nm in a liquid medium.<sup>41</sup> Some fine colloids can be translucent due to Tyndall scattering. Therefore, the electrochemical formation of LiF

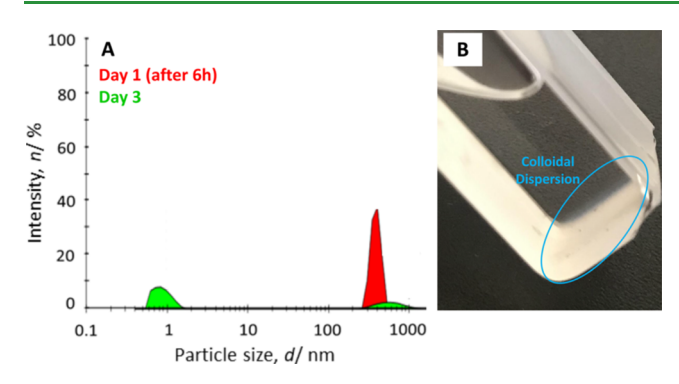


**Figure 4.** (A) DLS measurements of the LiF particle size over an aging period of 3 days in the electrolyte, containing 0.75 M LiBF<sub>4</sub> PC/DME 3:7 vol % and 0.1 M LiF at 25 °C. (B) Optical photograph of the DLS cuvette, revealing a hazy gel-like deposit at the bottom after 8 days, which appears to be a colloidal dispersion.

during discharge and the dispersion of LiF into the electrolyte upon aging are two competing rate processes, which influence the lithium-ion charge transfer at the  $CF_x$  electrode–electrolyte interface and explain the existence of impedance maxima in the EIS data (Figure 3D,F).

**Thermodynamic Analysis of Changes in Open-Circuit Potential.** Any changes in the thermodynamic activities of the reactants or products, including LiF, would be expected to change the open-circuit potential (OCP) of the cell. Indeed, a Li-CF<sub>x</sub> cell discharged to 3% DOD, heat-treated at 55 °C for 40 h, and then aged for 24 days shows an increase in the OCP (Figure S4B). To correlate the change of LiF particle size on the CF<sub>x</sub> electrode with the OCP, we formulate the Nernst equation  $^{42,43}$  for the overall electrochemical reaction (eq 3) when x = 1, yielding

$$E = E^{\circ} - \frac{RT}{zF} \ln \left( \frac{a_{\text{LiF}} a_{\text{C}}}{a_{\text{CF}} a_{\text{Li}}} \right) = E^{\circ} - \frac{RT}{zF} \ln(a_{\text{LiF}})$$
(4)

where E is the potential,  $E^{\circ}$  is the standard potential, R is the universal gas constant, T is the temperature, F is Faraday's constant, z is the number of transferred electrons, and a is the activity of the reactants and products. The activities of pure solids (C and Li) are unity, while we assume that the activity of solid CF is also unity. Thus, the cell potential E depends upon the activity of LiF,  $a_{\rm LiF}$ .

The chemical potential  $\mu_{\rm LiF}$  of LiF can be written in terms of its activity,

$$\mu_{\rm LiF} = \mu_{\rm LiF}^{\circ} + RT \ln(a_{\rm LiF}) \tag{5}$$

where  $\mu_{\rm LiF}^{\circ}$  is the chemical potential of LiF in its standard state. We further assume that the colloidal LiF in the electrolyte and solid LiF in the electrode are in equilibrium.

The Kelvin equation, <sup>41</sup> written in terms of chemical potentials, relates the chemical potential  $\mu_{\rm LiF}$  to the LiF particle radius r, the surface tension  $\kappa$  of LiF in the electrolyte, and the molar volume  $V_{\rm m}$  of LiF, according to

$$\mu_{\rm LiF} = \mu_{\rm LiF}^{\circ} + \frac{2\kappa V_{\rm m}}{r} \tag{6}$$

Changes in the chemical potential and LiF particle size can then be related by equating eqs 5 and 6

$$\frac{2\kappa V_{\rm m}}{r} = RT \ln(a_{\rm LiF}) \tag{7}$$

Solving for  $a_{LiF}$  and inserting it into the Nernst eq (eq 4) yields an expression for how the cell potential E relates to the LiF particle radius r

$$E = E^{\circ} - \frac{2\kappa V_{\rm m}}{zFr} \tag{8}$$

The OCP of the Li- $CF_x$  cell is therefore indirectly proportional to the radius r of the LiF particle. Thus, a decrease in the LiF particle radius would be expected to increase the OCP. This thermodynamic analysis therefore corroborates the experimentally obtained increase in the OCP of the Li- $CF_x$  cell over time (Figure S4B), which appears to occur due to LiF dispersion.

**Visualization of LiF Dispersion.** The changes in the  $CF_x$  surface during the aging period were also visualized by *operando* optical light microscopy. To do so, a  $CF_x$  electrode was immersed in the electrolyte and sealed under argon between two microscopy glasses (Figure 5A). The  $CF_x$ 

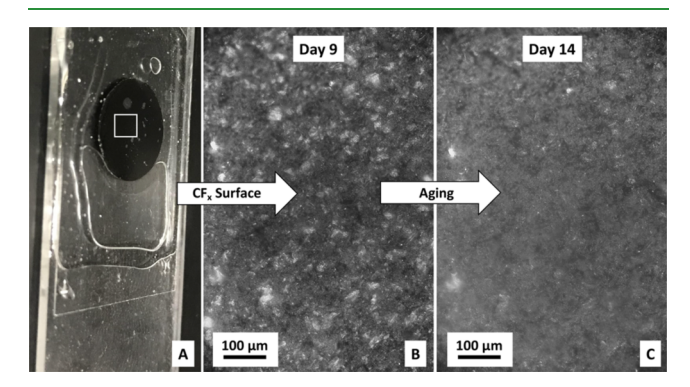


**Figure 5.** (A)  $CF_x$  electrode discharged to 3% DOD immersed in 0.75 M LiBF<sub>4</sub> PC/DME 3:7 vol % electrolyte and sealed under argon atmosphere between microscopy glass. Optical microscopy images of the exact same  $CF_x$  surface after (B) 9 and (C) 14 days of aging reveal that the surface morphology smoothed and LiF (light areas) disappeared.

electrode was previously discharged to 3% DOD in a coin cell, heat-treated, and aged for 9 days. The exact same surface of the  $CF_x$  electrode was captured at day 9 (Figure 5B) and day 14 (Figure 5C) of aging. The surface morphology at day 9 shows  $CF_x$  particles and LiF (light areas). After 14 days of aging, the surface morphology considerably smoothed, showing almost no LiF. These data support the above results, which indicate LiF disperses into the electrolyte within 14 days of aging.

The evolution of LiF during discharge and aging is summarized schematically in Figure 6. LiF forms as an electrochemical discharge product on the  $CF_x$  electrode, which grows as the discharge proceeds, forming a resistive layer. LiF subsequently disperses into the organic electrolyte during aging, though it does not solubilize at the molecular level. Rather, experiments suggest that LiF forms a colloidal dispersion.

Application of In-Line EIS to Determine the DOD of Li-CF<sub>x</sub> Cells. As compared to other Li-based batteries, Li-CF<sub>x</sub> has a very flat discharge plateau around 2.6 V, which poses a challenge for the accurate determination of the battery cell DOD by coulomb counting alone. These features are observed in the galvanostatic discharge curve of a two-electrode Li-CF<sub>x</sub> cell discharged to 1.5 V at a rate of C/120 at 20 °C (Figure S8). To address this problem, we correlate the impedance of

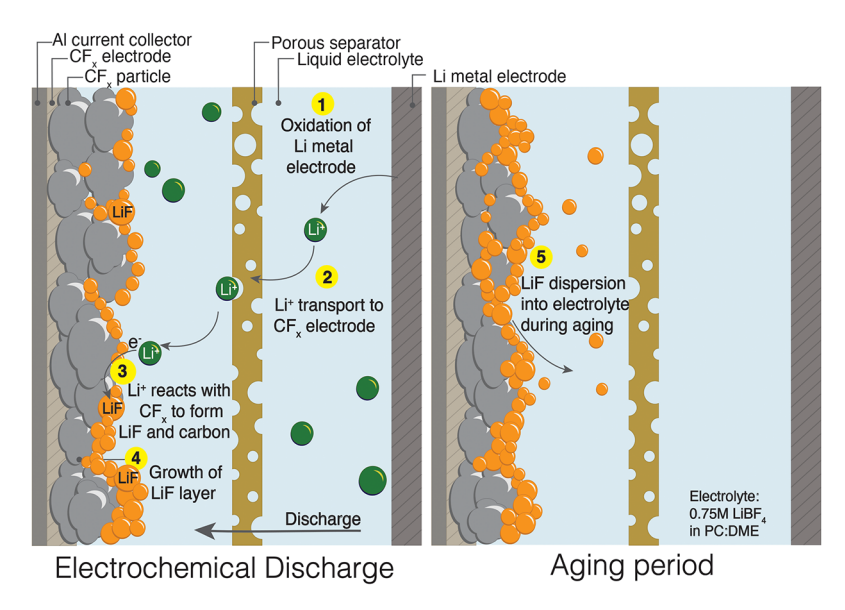


Figure 6. Schematic illustrating (left) the electrochemical discharge of a Li- $CF_x$  cell, including the formation and growth of LiF on the  $CF_x$  electrode, and (right) the subsequent dispersion of LiF into the organic electrolyte during aging, which notably does not solubilize at a molecular level.

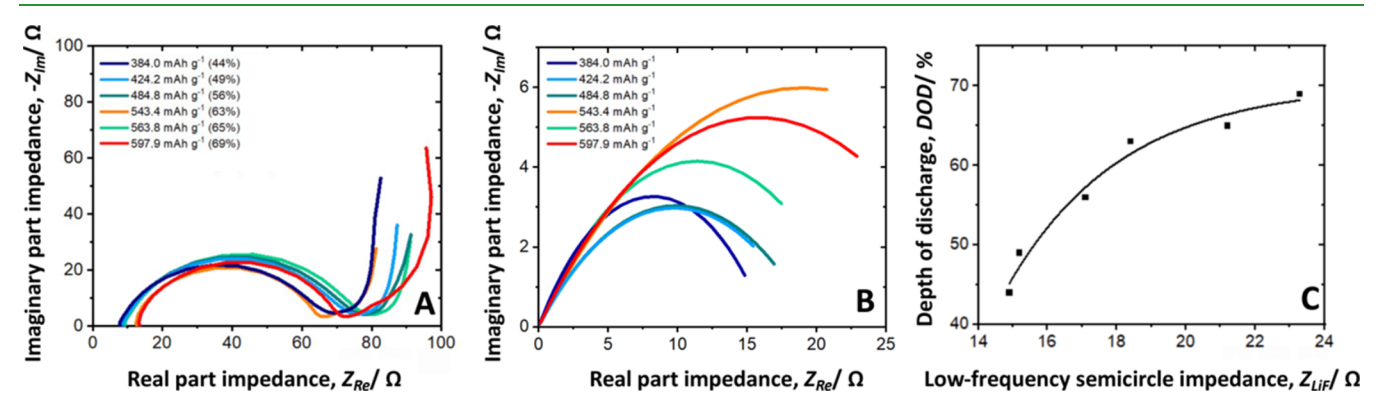


Figure 7. In-line EIS method to determine DOD beyond coulomb counting. (A) Complex plane plots of a Li-CF $_x$  coin cell discharged to different DOD obtained by in-line GEIS. Before discharge, the coin cell was discharged to 3% DOD, heat-treated at 55 °C for 40 h, and then aged for 14 days to account for LiF dispersion in the electrolyte and aging of the LiF layer. (B) Disentangled low-frequency semicircle  $(Q_3/R_3)$ , representing the LiF layer of the Li-CF $_x$  coin cells at different DODs. (C) Relationship between the DOD and the low-frequency semicircle  $(Q_3/R_3)$  impedance of the coin cells, which follows an exponential decay process.

the low-frequency semicircle, which is a measurable quantity indicative of how the LiF layer evolves with increasing DOD. Since we know that Li-CF $_x$  cells experience an aging process over a period of ca. 14 days that changes the interface of the CF $_x$  electrode, we must first eliminate any competing rate processes associated with LiF dispersion in the electrolyte and concomitant changes in the LiF layer before galvanostatically discharging the cells. For the cells studied here, this result can be achieved by ensuring that after initial discharge (3% DOD) and heat treatment, the cell is aged for at least 14 days before taking EIS measurements. We then assume that the growth of the LiF layer and thus the increase of the low-frequency semicircle diameter will be the only rate process during discharge in aged cells.

To test this assumption, we galvanostatically discharged aged Li-CF<sub>x</sub> coin cells and immediately performed GEIS at different DODs Table S1 without allowing the cells to rest (Figure 7A). The trend of the low-frequency semicircle impedance  $(Q_3/R_3)$  (Figure 7B) at different DOD follows an exponential decay process according to DOD =  $100 \times (1 - 1)$ 

 $\exp(-\alpha \times Z)$ ), where  $\alpha$  is a constant that likely depends upon cell physical parameters (e.g., mass loading) and (Figure 7C). The real impedance of the low-frequency semicircle was obtained by determining the diameter of the fitted Q/R element. Thus, in-line EIS can be used as a method to determine the DOD while taking the impedance of the lowfrequency semicircle  $(Q_3/R_3)$  as a marker for the DOD. Before doing so, the electrolyte must be saturated with dispersed LiF from the CF<sub>x</sub> cathode to eliminate any competing rate processes caused by aging of the LiF blocking layer. Note that the electrolyte in the coin cells studied here is "saturated" with LiF at a DOD of approximately 7-11%, depending on the active cathode mass. In general, LiF dispersion, saturation, and aging must be considered during the pretreatment of the Li-CF<sub>x</sub> battery for this method of DOD determination can be used.

Quantitative Molecular-Level Understanding of Li-CF<sub>x</sub> Reaction Mechanism. To elucidate the molecular-level evolution of electrochemically formed LiF and the CF bonds during discharge, we acquired solid-state <sup>19</sup>F MAS NMR spectra of cells at different DOD values following the EIS measurements (Figure 8). Upon discharge, both covalent CF

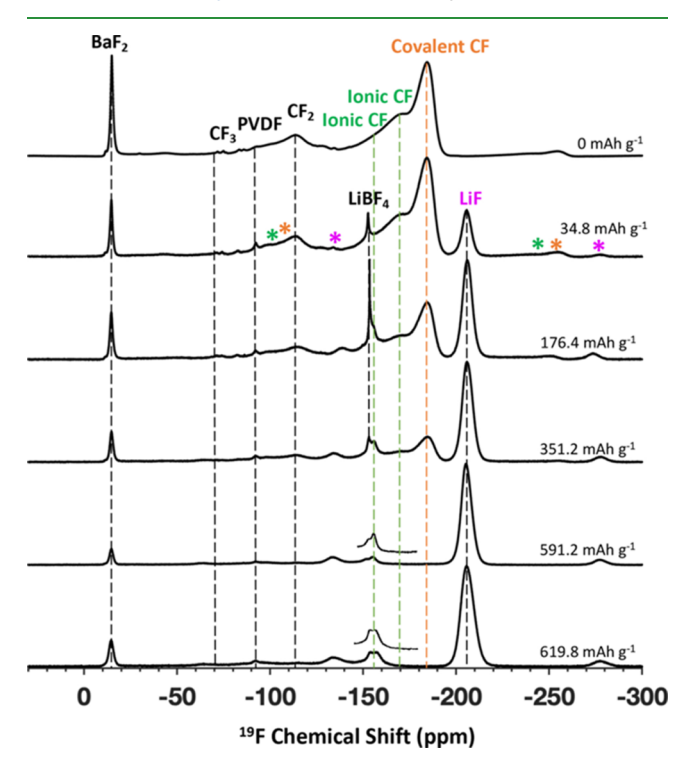


Figure 8. Solid-state <sup>19</sup>F MAS NMR spectra of CF<sub>x</sub> electrodes from Li-CF, coin cells galvanostatically discharged to different DODs. Spinning side bands are labeled as follows: ionic CF = green, covalent CF = orange, and LiF = pink. BaF<sub>2</sub> was added as an internal <sup>19</sup>F reference.

and ionic CF moieties decrease in signal intensity as the LiF signal increases, demonstrating that CF bonds are electrochemically reduced and react with Li<sup>+</sup> to form LiF (eq 3). Interestingly, a remaining <sup>19</sup>F CF signal centered around -156 ppm is observed even after 1.5 V, which is associated with CF bonds that have the most ionic character. Note that the 19F signal at -154 ppm associated with residual LiBF<sub>4</sub> salt was observed in multiple  $CF_x$  electrodes (those discharged to 34.8, 176.4, and 351.2 mAh g<sup>-1</sup>). Solid-state <sup>7</sup>Li MAS NMR spectra were also obtained (Figure S7), showing the electrochemical formation of LiF, as expected.

The solid-state <sup>19</sup>F MAS NMR spectra were deconvoluted into individual <sup>19</sup>F signals, enabling their relative populations to be quantified (Figure 9, Table 1). The <sup>19</sup>F spinning side bands, as well as solid-state  $^{19}\mathrm{F}$  transverse relaxation  $(T_2)$  filters, aided in identifying the  $^{19}\mathrm{F}$  chemical shifts and line widths of overlapping signals. The molar percentage of LiF obtained from each electrode was compared to the DOD, i.e., the fraction of specific capacity extracted relative to a maximum theoretical value of 865 mAh g<sup>-1</sup>. The NMR and electrochemical results are thus in excellent quantitative agreement, with the former also providing molecular-level specificity into the electrochemical transformations that occur with increasing DOD. With regard to LiF, the results show that the molar percentage of LiF formed follows a similar exponential decay process with increasing DOD (Figure 7C), confirming our EIS observations. Note that full theoretical specific capacity was not achieved using these in-house Li-CF<sub>x</sub> cells, which could be experimentally optimized further.

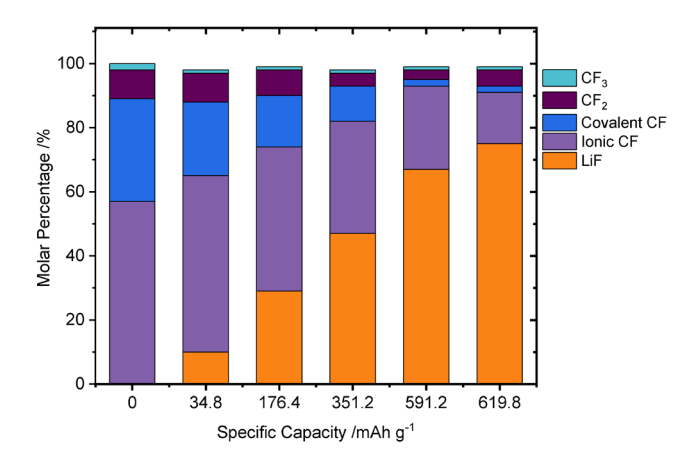


Figure 9. Molar percentages of <sup>19</sup>F moieties obtained from deconvoluting solid-state 19F MAS NMR spectra of the CF<sub>x</sub> electrodes discharged to different DOD.

Table 1. Comparison of the Specific Capacity Extracted, DOD, and Molar Percentages Obtained from Solid-State <sup>19</sup>F MAS NMR Spectra

		molar percentage (%)		
specific capacity (mAh $g^{-1}$ )	DOD <sup>a</sup> (%)	LiF	ionic CF	covalent CF
0	0	0	57	32
34.8	4	10	55	23
176.4	20	29	45	16
351.2	41	47	35	11
591.2	68	67	26	2
619.8	72	75	16	2

<sup>a</sup>DOD computed with respect to the theoretical specific capacity of  $CF_x (x = 1)$ , 865 mAh g<sup>-1</sup>.

Commercial Li-CF<sub>x</sub> cells typically achieve >90% of theoretical

Additional molecular-level insight into the electrochemical discharge mechanism of Li-CF<sub>x</sub> cells is revealed by analyzing how the relative populations of covalent and ionic CF bonds evolve upon increasing the DOD. As the cell is discharged, covalent CF is first preferentially consumed, a possible consequence of the weaker bond strength of covalent versus ionic CF bonds. Then, as the electrochemical reduction of CF bonds proceeds, ionic CF bonds are broken alongside covalent CF bonds, where the latter are almost completely consumed. As mentioned above, not all of the CF bonds were electrochemically reduced to LiF, as revealed by the remaining  $^{19}\mathrm{F}$  CF signal centered at -156 ppm. The existence of remaining CF bonds is consistent with the extracted specific capacity upon galvanostatic discharge to 1.5 V (Table 1), which indicates that less than the theoretical capacity was extracted. The experimental data thus suggest that CF bonds of the most ionic character, which are expected to be the strongest CF bonds, are the limiting factors in achieving the full theoretical specific capacity.

## **CONCLUSIONS**

The interfacial and molecular-level changes that occur in CF<sub>x</sub> electrodes were investigated upon electrochemical discharge and aging of Li-CF<sub>x</sub> cells and studied by correlated EIS and solid-state NMR measurements. We identified and disentangled the different impedance contributions associated with

the CF<sub>r</sub> electrode based on their frequency responses, including a contribution ascribed to LiF. We discovered that electrochemically formed LiF on the CF<sub>x</sub> surface disperses partially into the electrolyte, forming a colloidal dispersion within ca. 14 days of aging. Electrochemical LiF formation and concomitant LiF dispersion in the electrolyte results in two distinct, competing rate processes that increase and decrease cell impedance, respectively, which can result in nonmonotonic changes of the cell impedance depending on cell DOD, rest periods, and saturation of LiF in the electrolyte. LiF dispersion is supported by DLS measurements, revealing the reduction of particle size of crystalline LiF within 6 h after mixing with the electrolyte, containing 0.75 M LiBF<sub>4</sub> PC/DME 3:7 vol %. In addition, optical microscopy imaging of the CF<sub>x</sub> electrode surface showed an apparent smoothing of the surface morphology, suggesting the dispersion of interfacial LiF upon aging. Liquid-state <sup>7</sup>Li and <sup>19</sup>F NMR measurements of the pristine electrolyte, as well as electrolyte aged for 24 h after the addition of 1 M LiF reveal that LiF is not solubilizing at a molecular level, a result corroborated by the specific conductivity measurements. The dispersion of electrochemically formed LiF on CF<sub>x</sub> into the electrolyte increases the OCP of the Li-CF<sub>x</sub> cell, as shown by experimental data and thermodynamic analysis using the Nernst and Kelvin equations.

After saturation of the electrolyte with dispersed LiF, the growth of the LiF layer on the surface of CF<sub>r</sub> was then the only significant rate process during discharge, allowing for the impedance contributions of the LiF layer to be associated with the DOD of the Li-CF<sub>x</sub> battery. GEIS measurements of aged cells revealed that the LiF layer impedance follows an exponential decay process. The molar percentage of LiF obtained by solid-state <sup>19</sup>F nuclear NMR measurements was compared to that of the DOD, confirming the impedance increase due to LiF formation. Furthermore, we show that covalent CF is first preferentially consumed during discharge and ionic CF bonds are broken alongside covalent CF bonds. Interestingly, CF bonds were not entirely electrochemically reduced to LiF even after full discharge to 1.5 V. This is associated with CF bonds that have the most ionic character, which are expected to be the strongest CF bonds and thus are the limiting factor in achieving the full theoretical specific capacity in Li-CF<sub>x</sub> cells. Overall, the results provide mechanistic insights into the molecular-level changes in Li-CF<sub>x</sub> batteries, particularly the formation and distribution of LiF, as well as inform clear guidelines for the cell pretreatment, enabling determination of the battery's DOD. The results may also have implications for lithium metal battery systems beyond Li-CF<sub>x</sub>, depending on the electrolyte used, as LiF commonly forms in solid electrolyte interphases.

# ASSOCIATED CONTENT

#### Supporting Information

The Supporting Information is available free of charge at https://pubs.acs.org/doi/10.1021/acsami.3c17562.

> Solid-state 19F NMR spectra at different MAS rates; complex plane plots of two-electrode and threeelectrode cell configurations; models of complex plane plots; correlation of two-electrode and three-electrode cell complex plane plots; specific conductivity measurements; open-circuit potential measurements; liquid-state <sup>1</sup>H and <sup>7</sup>Li NMR measurements; images of LiF mixed

with pristine electrolyte; solid-state <sup>7</sup>Li NMR spectra; and galvanostatic discharge curves of Li-CF<sub>x</sub> cells (PDF)

#### AUTHOR INFORMATION

#### **Corresponding Author**

Robert J. Messinger - Department of Chemical Engineering, The City College of New York, CUNY, New York, New York 10031, United States; orcid.org/0000-0002-5537-3870; Email: rmessinger@ccny.cuny.edu

#### **Authors**

Theresa Schoetz - Department of Chemical Engineering, The City College of New York, CUNY, New York, New York 10031, United States; orcid.org/0000-0002-0016-4238

Loleth E. Robinson – Department of Chemical Engineering, The City College of New York, CUNY, New York, New York 10031, United States; orcid.org/0009-0007-6991-9401

Leo W. Gordon - Department of Chemical Engineering, The City College of New York, CUNY, New York, New York 10031, United States; orcid.org/0000-0002-8242-9470

Sarah A. Stariha – Jet Propulsion Laboratory, California Institute of Technology, Pasadena, California 91109, United States

Celia E. Harris - Department of Chemical Engineering, The City College of New York, CUNY, New York, New York 10031, United States

Hui Li Seong – Jet Propulsion Laboratory, California Institute of Technology, Pasadena, California 91109, United States

John-Paul Jones – Jet Propulsion Laboratory, California Institute of Technology, Pasadena, California 91109, United

Erik J. Brandon – Jet Propulsion Laboratory, California Institute of Technology, Pasadena, California 91109, United States; orcid.org/0000-0001-6106-7645

Complete contact information is available at: https://pubs.acs.org/10.1021/acsami.3c17562

#### **Author Contributions**

§T.S. and L.E.R. contributed equally to this work.

The authors declare no competing financial interest.

#### **ACKNOWLEDGMENTS**

T.S., L.E.R., and R.J.M. gratefully acknowledge funding from the U.S. National Aeronautics and Space Administration (NASA) via the NASA-CCNY Center for Advanced Batteries for Space under cooperative agreement 80NSSC19M0199. L.W.G. and R.J.M thank the U.S. National Science Foundation (NSF) for support through NSF CAREER award CBET-1847552. Part of this research was carried out at the Jet Propulsion Laboratory, California Institute of Technology, under a contract with the National Aeronautics and Space Administration (#80NM0018D0004). This work was partially supported by the NASA Science Mission Directorate. The information presented about future NASA mission concepts is predecisional and is provided for planning and discussion purposes only. The authors thank Brendan Hawkins from The City College of New York (CCNY) for his assistance with the optical microscopy setup and measurements. Solid-state NMR measurements were performed at the City University of New York (CUNY) Advanced Science Research Center. Liquidstate NMR measurements were performed at the CCNY

Center for Discovery and Innovation and were made possible by equipment purchased through NSF Major Research Instrumentation (MRI) award 2117799.

#### REFERENCES

- (1) Read, J.; Collins, E.; Piekarski, B.; Zhang, S. LiF Formation and Cathode Swelling in the Li/CF x Battery. *J. Electrochem. Soc.* **2011**, 158 (5), A504—A510.
- (2) Sayahpour, B.; Hirsh, H.; Bai, S.; et al. Revisiting Discharge Mechanism of CFx as a High Energy Density Cathode Material for Lithium Primary Battery. *Adv. Energy Mater.* **2022**, *12* (5), 2103196 DOI: 10.1002/aenm.202103196.
- (3) Li, L.; Zhang, S.; Chen, C.; Xu, C.; Wang, R.; Wu, M. Potassium Ion Electrolytes Enable High Rate Performance of Li/CFx Primary Batteries. *J. Electrochem. Soc.* **2023**, *170* (4), No. 040506.
- (4) Gao, H.; Sevilla, A. R.; Hobold, G. M.; et al. Fluoro-Organosulfur Catholytes to Boost Lithium Primary Battery Energy. *Proc. Natl. Acad. Sci. U.S.A.* **2022**, *119* (45), e2121440119 DOI: 10.1073/pnas.2121440119.
- (5) Gao, H.; Yoshinaga, K.; Steinberg, K.; Swager, T. M.; Gallant, B. M. Cascade Defluorination of Perfluoroalkylated Catholytes Unlocks High Lithium Primary Battery Capacities. *Adv. Energy Mater.* **2023**, *13* (32), 2301751 DOI: 10.1002/aenm.202301751.
- (6) Krishnamurthy, V.; Viswanathan, V. Beyond Transition Metal Oxide Cathodes for Electric Aviation: The Case of Rechargeable CFx. ACS Energy Lett. 2020, 5 (11), 3330–3335.
- (7) Yin, Y.; Holoubek, J.; Liu, A.; et al. Ultralow-Temperature Li/CFx Batteries Enabled by Fast-Transport and Anion-Pairing Liquefied Gas Electrolytes. *Adv. Mater.* **2023**, *35* (3), 2207932 DOI: 10.1002/adma.202207932.
- (8) Linden, D.; Reddy, T. B. *Handbook of Batteries*, 3rd ed.; Thomas, R., Ed.; McGraw-Hill, 2001.
- (9) Jones, J. P.; Jones, S. C.; Billings, K. J.; et al. Radiation Effects on Lithium CFx Batteries for Future Spacecraft and Landers. *J. Power Sources* **2020**, 471, 228464 DOI: 10.1016/j.jpowsour.2020.228464.
- (10) Leung, K.; Schorr, N. B.; Mayer, M.; Lambert, T. N.; Meng, Y. S.; Harrison, K. L. Edge-Propagation Discharge Mechanism in CFx Batteries—A First-Principles and Experimental Study. *Chem. Mater.* **2021**, 33 (5), 1760–1770.
- (11) Giraudet, J.; Dubois, M.; Guérin, K.; et al. Solid-state 19F and 13C NMR of Room Temperature Fluorinated Graphite and Samples Thermally Treated Under Fluorine: Low-Field and High-Resolution Studies. *J. Solid State Chem.* **2005**, *178* (4), 1262–1268.
- (12) Panich, A. M.; Nakajima, T.; Goren, S. D. 19F NMR Study of C-F Bonding and Localization Effects in Fluorine-Intercalated Graphite. *Chem. Phys. Lett.* **1997**, *271* (4–6), 381–384.
- (13) Piraux, L.; Bayot, V.; Issi, J. P.; Dresselhaus, M. S.; Endo, M.; Nakajima, T. Electrical and thermal properties of fluorine-intercalated graphite fibers. *Phys. Rev. B* **1990**, 41 (8), 4961 DOI: 10.1103/PhysRevB.41.4961.
- (14) Davis, S.; Takeuchi, E. S.; Tiedemann, W.; Newman, J. Simulation of the Li-CFx System. *J. Electrochem. Soc.* **2007**, *154* (5), A477.
- (15) Krause, F. C.; Jones, J.-P.; Jones, S. C.; et al. High Specific Energy Lithium Primary Batteries as Power Sources for Deep Space Exploration. *J. Electrochem. Soc.* **2018**, *165* (10), A2312–A2320.
- (16) Smith, P. H.; Sepe, R. B.; Waterman, K. G.; Myron, L. J. Development and Analysis of a Lithium Carbon Monofluoride Battery-Lithium Ion Capacitor Hybrid System for High Pulse-Power Applications. *J. Power Sources* **2016**, 327, 495–506.
- (17) Hand, K. P.; Phillips, C. B.; Murray, A.; et al. Science Goals and Mission Architecture of the Europa Lander Mission Concept. *Planet. Sci. J.* 2022, 3 (1), 22.
- (18) Touhara, H.; Fujimoto, H.; Watanabe, N.; Tressaud, A. Discharge Reaction Mechanism in Graphite Gluoride-Lithium Batteries. *Solid State Ionics* **1984**, *14* (2), 163–170.

- (19) Bock, D. C.; Marschilok, A. C.; Takeuchi, K. J.; Takeuchi, E. S. Batteries Used to Power Implantable Biomedical Devices. *Electrochim. Acta* **2012**, *84*, 155–164.
- (20) Zhang, S. S.; Foster, D.; Wolfenstine, J.; Read, J. Electrochemical characteristic and discharge mechanism of a primary Li/CFx cell. *J. Power Sources* **2009**, *187* (1), 233–237.
- (21) Guérin, K.; Dubois, M.; Hamwi, A.Advanced Carbon Fluorides for Primary Lithium Batteries. In E3S Web of Conferences; EDP Sciences, 2017; p 17002.
- (22) Watanabe, N. Two Types of Graphite Fluorides, (CF)n and (C2F)n, and Discharge Characteristics and Mechanisms of Electrodes of (CF)n and (C2F)n in Lithium Batteries. *Solid State Ionics* **1980**, *1* (1–2), 87–110.
- (23) Arnot, D. J.; Takeuchi, E. S.; Marschilok, A. C.; Takeuchi, K. J. Isothermal Microcalorimetric Analysis of Li/CFx Battery Discharge. *J. Electrochem. Soc.* **2023**, *170* (6), No. 060505.
- (24) Whittingham, M. S. Mechanism of Reduction of the Fluorographite Cathode. J. Electrochem. Soc. 1975, 122 (4), 526–527.
- (25) Nagasubramanian, G.; Sanchez, B. A New Chemical Approach to Improving Discharge Capacity of Li/(CFx)n cells. *J. Power Sources* **2007**, *165* (2), 630–634.
- (26) Wu, M.; Li, M.; Jin, Y.; et al. In situ formed LiF-Li3N Interface Layer Enables Ultra-Stable Sulfide Electrolyte-Based All-Solid-State Lithium Batteries. *J. Energy Chem.* **2023**, *79*, 272–278.
- (27) Xie, J.; Zhao, M.; Wang, C.; Yong, Y.; Gu, Z. Recent Advances in Understanding the Effects of Nanomaterials on Gut Microbiota. *Chem. Eng. J.* **2022**, 435 (P3), No. 134976.
- (28) Liu, Z.; Guo, D.; Fan, W.; Xu, F.; Yao, X. Expansion-Tolerant Lithium Anode with Built-In LiF-Rich Interface for Stable 400 Wh kg-1 Lithium Metal Pouch Cells. *ACS Mater. Lett.* **2022**, 4 (8), 1516–1522.
- (29) Jow, T. R.; Delp, S. A.; Allen, J. L.; Jones, J.-P.; Smart, M. C. Factors Limiting Li+ Charge Transfer Kinetics in Li-Ion Batteries. *J. Electrochem. Soc.* **2018**, *165* (2), A361–A367.
- (30) Massiot, D.; Fayon, F.; Capron, M.; et al. Modelling One- and Two-Dimensional Solid-State NMR Spectra. *Magn. Reson. Chem.* **2002**, *40* (1), 70–76.
- (31) Guo, R.; Kim, K.-H.; Gallant, B. M. Impact of LiF Particle Morphology on Overpotential and Structure of Li Metal Deposition. *J. Electrochem. Soc.* **2022**, *169* (10), No. 100523.
- (32) Krawietz, T.; Haw, J. Characterization of poly(carbon monofluoride) by 19 and 19 F to 13 C cross polarization MAS NMR spectroscopy. *Chem. Commun.* **1998**, *19*, 2151–2152, DOI: 10.1039/A803252A. Published online
- (33) DeSilva, J. H.; Vazquez, R.; Stallworth, P. E.; et al. Solid-State Nuclear Magnetic Resonance Studies of Electrochemically Discharged CFx. *J. Power Sources* **2011**, *196* (13), 5659–5666.
- (34) Leifer, N. D.; Johnson, V. S.; Ben-Ari, R.; et al. Solid-State NMR Studies of Chemically Lithiated CFx. J. Electrochem. Soc. 2010, 157 (2), A148.
- (35) Kim, K. H.; Cho, J. H.; Hwang, J. U.; Im, J. S.; Lee, Y. S. A Key Strategy to Form a LiF-based SEI Layer for a Lithium-Ion Battery Anode With eEhanced Cycling Stability by Introducing a Semi-Ionic C–F Bond. *J. Ind. Eng. Chem.* **2021**, *99*, 48–54.
- (36) Chen, P.; Liu, W.; Wang, H.; Jiang, Y.; Niu, X.; Wang, L. Semi-Ionic C-F Bond Enabling Fluorinated Carbons Rechargeable as Li-Ion Batteries Cathodes. *J. Colloid Interface Sci.* **2023**, 649, 255–263.
- (37) Giraudet, J.; Dubois, M.; Guérin, K.; Delabarre, C.; Hamwi, A.; Masin, F. Solid-state NMR Study of the Post-Fluorination of (C2.5F)n Fluorine GIC. *J. Phys. Chem. B* **2007**, *111* (51), 14143–14151.
- (38) Holstein, P.; Harris, R. K.; Say, B. J. Solid-state 19F NMR Investigation of Poly(Vinylidene Fluoride) With High-Power Proton Decoupling. *Solid State Nucl. Magn. Reson.* **1997**, 8 (4), 201–206.
- (39) Seong, H. L.; Ruiz, J. P.; Jones, J.-P.; et al. Anomalous Behavior During Low Rate Discharge of Li/CFx Cells. *J. Electrochem. Soc.* **2022**, 169 (6), No. 060550.
- (40) Jones, J.; Anouti, M.; Caillon-Caravanier, M.; Willmann, P.; Lemordant, D. Thermodynamic of LiF dissolution in Alkylcarbonates

and Some of Their Mixtures With Water. Fluid Phase Equilib. 2009, 285 (1-2), 62-68.

- (41) Hiemenz, P. C.; Rajagopalan, R. Principles of Colloid and Surface Chemistry, 3rd ed.; Marcel Dekker, 1997.
- (42) Bard, A.; Faulkner, L. Electrochemical Methods Fundamentals and Applications, 2nd ed.; John Wiley & Sons, 2001.
- (43) Balsara, N.; Newman, J. Electrochemical Systems, 4th ed.; John Wiley & Sons, 2021.